International Journal of Heat and Mass Transfer 117 (2018) 1158–1168

Contents lists available at ScienceDirect

International Journal of Heat and Mass Transfer

journal homepage: www.elsevier.com/locate/ijhmt

Flow-boiling canopy wick for extreme heat transfer

Minki Kim, Massoud Kaviany *

Department of Mechanical Engineering, University of Michigan, Ann Arbor, MI 48109, USA

ARTICLE INFO

Article history:
Received 7 August 2017
Received in revised form 17 October 2017
Accepted 19 October 2017
Available online 5 November 2017

Keywords:
Boiling metamedium
Boiling heat flux and conductance limits
Vapor venting
Two-phase flow stability

ABSTRACT

The maximum theoretical boiling heat transfer rate q_{max} is set by interface unidirectional thermal vapor flux, and quest continues for achieving a high fraction of it under saturated liquid flow. We introduce the flow-boiling canopy wick (FBCW) employing film (meniscus) evaporation and perforated screenlayer separating the liquid stream from the underlying vapor space. The vapor vents continuously through periodic perforations, in contrast to plain surface which becomes completely covered by vapor at high heat flux. The FBCW allows streamwise liquid tracks on the screenlayer between perforations providing capillary liquid flow toward heated surface and evaporation on high-effective-conductivity monolayer wick. Under extreme heat flux, various hydrodynamic limits prevent liquid supply and vapor removal, i.e., the capillary-viscous, wick superheat, perforation pressure drop and chocking and liquid-vapor stability limits. The liquid and vapor inertiae control the streamwise continuous liquid track (with isolated and/or merged vapor track) and for saturated water at 1 atm CFD and wick pressure drop predict heat flux up to $0.1q_{max}$ = 20 MW/m^2, an order-of-magnitude larger than the nucleate flow-boiling limit. The concept of replacing the chaotic nucleated bubbles with the structured, continuous vapor venting in the periodic FBCW transforms boiling heat transfer and its upper limit.

1. Introduction and flow-boiling canopy wick

Boiling heat flux limit is governed by the supply of heat and liquid for evaporation, and removal of vapor (allowing for liquid irrigation), with the upper limit set by the maximum vapor flow rate predicted by the kinetic theory of gases. The surface-convection thermal-hydraulic limitations by boundary layers and liquid-vapor phase competition can be controlled using 3-D multiscale, unit-cell based boiling metamedium. The metamedium combines (a) high-effective-thermal-conductivity capillary monolayer for evaporation, (b) high-permeability liquid supply posts separating the liquid and vapor phases, and flows, and (c) uniquely designed liquid- and vapor-tracks – leading to record high heat flux and thermal conductance. Metamaterials are engineered (synthesized from multiple elements in repeating patterns) to provide properties not naturally available employing heterogeneities for effective macroscopic transport (e.g., multiscale function-designed porous media).

While low thermal resistance has been observed for subcooled boiling, the saturated flow boiling, even at very large liquid speed (up to 10 m/s), has not yet been able to reach the low thermal resistance achieved with multidimensional wicks under saturation. Based a review of boiling in coated surface [1], here we introduce a multiscale 3-D flow-boiling canopy wick (FBCW) for achieving low thermal resistance and high critical heat flux (CHF) in boundary-layer flow boiling. The selection of flow conditions is to initially avoid the effect of the channel hydraulic diameter, although it should be mentioned that this wick has dimension of the order of millimeter, so it is suitable for multi-millimeter and larger channels (for thermal management and vapor production). The structure allows for film evaporation over a thin porous-layer coating called the monolayer, as shown in Fig. 1. The structure is periodic in two directions, and its simplest unit cell will contain four posts, a screenlayer (two or three layers) acting as roof with a centered perforation, and a thin porous layer making the floor of the canopy wick. While thin, this layer has an optimal combination of permeability and maximum capillary pressure to spread the liquid supplied through the high permeability posts. The aim is to create and maintain a vapor space for steady and uniform film evaporation, while allowing for liquid supply and vapor escape.

2. Flow-boiling heat flux and conductance limits

The available results on maximum heat flux (q), and heat transfer coefficient or specific conductance (G/A) for plain and coated surfaces, under pool boiling (PB) [2–7], flow boiling (FB, no subcooling) [8–10], and with multi-artery heat-pipe spreader

* Corresponding author.
E-mail address: kaviany@umich.edu (M. Kaviany).

https://doi.org/10.1016/j.ijheatmasstransfer.2017.10.079
0017-9310/

Nomenclature

A	area (m^2)
C, c	coefficients
c_d	discharge coefficient
c_p	heat capacity (J/kg-K)
D, d	diameter (m)
Fr	Froude number
f	friction coefficient, force
G/A	heat transfer coefficient (W/m^2-K)
g	gravitational acceleration (m/s^2)
H	height (m)
Δh_{lg}	heat of evaporation (kJ/kg)
K	permeability (m^2)
k	thermal conductivity (W/m-K)
k_B	Boltzmann constant (J/K)
L	length, pitch, thickness (m)
M	mass (kg)
Ma	Mach number
m	molecular mass (g/mol)
N_{per}	ratio of monolayer unit cell per perforation
N_p	packing number
n_{sh}	number density of shute wire ($1/in^2$)
n_{wa}	number density of warp wire ($1/in^2$)
p	pressure (Pa)
Q	heat flow rate (W)
q	heat flux (W/m^2)
R	thermal resistance (K/W)
Re	Reynolds number
r	radial location, radius (m)
s	substrate, saturation
T	temperature (K)
u	velocity (m/s)
v	velocity (m/s)
W, w	width (m)
We	Weber number
x	quality, position in streamwise direction (m)
$\langle\rangle$	average

Greek symbols

α	gas void fraction
β	ratio of perforation area to area before perforation
Δ	difference, drop
δ_l	liquid thickness (m)
ϵ	porosity
γ	heat capacity ratio
κ_g	gas interface curvature (1/m)
λ	wavelength (m)
λ_m	pitch of permeable periodic stacks (m)
μ	viscosity (Pa-s)
ρ	density (kg/m^3)
σ	surface tension (N/m)
θ_c	contact angle (°)

Subscripts

ac	cross-sectional
CHF	critical heat flux
c	capillary, channel, cooling, cross
cr	critical
$c\text{-}v$	capillary-viscous
e	effective, evaporator
FB	flow boiling
g	gas
h	heated
I	isolated
i	index of node, inlet
l	liquid
lg	liquid-gas phase change
$l-g, st$	liquid-gas stability
M	merged
m	monolayer wicks
max	maximum
N	total number of nodes
o	opening
PB	pool boiling
p	post (artery)
per	perforation
po	pore
s	screen mesh, surface, surface tension
sh	shute wire
t	thermal
u	fluid flow
wa	warp wire
Z	Zuber
$\updownarrow$	across
$\leftrightarrow$	along

(MAHPS) [1] are shown in Fig. 2, for water at 1 atm. The surface-convection conductance for impinging jet is based on the results of [11] and review in [12]. Since the surface-convection resistance is in series with the substrate conduction resistance, the conduction conductance is also shown (under copper or synthetic diamond as material). The predicted superior performance [q up to 20 MW/m^2 and (G/A) over 0.2 MW/m^2-K] of the proposed FBCW is also shown. In general, coatings and nano/microstructures reduce the surface superheat $T_s - T_{lg}$ (T_{lg} is saturation temperature) by either increasing the nucleation sites or creating film evaporation over thin, high effective conductivity wicks. They also tend to enhance the CHF governed by the liquid-vapor hydrodynamic instability or the capillary-viscous limit of liquid flow through porous bodies. The vapor escaping paths are more readily accommodated, but vapor chocking limit can occur.

The maximum theoretical heat flux is based on the interfacial, unidirectional thermal flux of vapor q_{max} [13–15]

$$q_{max} = \rho_g \Delta h_{lg} (k_B T_{lg}/2\pi m)^{1/2}, \tag{1}$$

with ρ_g vapor density, Δh_{lg} heat of evaporation, k_B Boltzmann constant, and m average molecular mass. This Schrage formulation-relation has been critically reviewed by [14], but the perturbative non-equilibrium corrections are not easily incorporated and also not very significant.

The modulated wick in pool boiling allows control of the instability wavelength with the pitch of permeable periodic stacks λ_m [2] shown in Fig. 2 with the CHF as

$$\frac{q_{CHF,PB}}{\pi/24\rho_g^{1/2}\Delta h_{lg}[\sigma g(\rho_l-\rho_g)]^{1/4}} = \frac{3[\sigma/g(\rho_l-\rho_g)]^{1/4}}{\lambda_m^{1/2}}, \tag{2}$$

with ρ_l liquid density, σ surface tension, and g gravitational acceleration. For plain surface this wavelength is governed by fluid properties (in the Zuber hydrodynamic limit $q_{CHF,Z}$), i.e.,

$$\lambda_m = 9[\sigma/g(\rho_l-\rho_g)]^{1/2}. \tag{3}$$

The flow-boiling limit $q_{CHF,FB,1}$ is given by empirical relation [9]

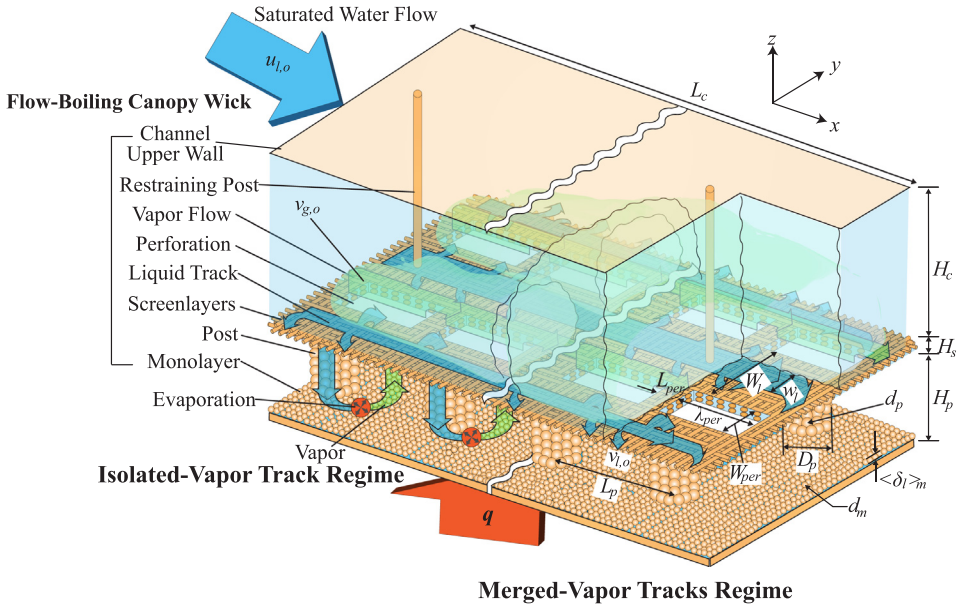

Fig. 1. Schematic of FBCW showing the multiscale (monolayer, posts, and screenlayer), 3-D wick structures and vapor venting from screenlayer perforations into crossing liquid flow. The geometric parameters are also shown. The upstream, isolated vapor tracks and downstream, merged vapor tracks are shown.

$$\frac{q_{CHF,FB,1}}{\rho_l u_{l,o} \Delta h_{lg}} = C_1 \mathrm{We}_{D,c}^{C_2} (\rho_l/\rho_g)^{C_3} \times \frac{[1 - C_4 (\rho_l/\rho_g)^{C_5} x_i]}{1 + 4 C_1 C_4 \mathrm{We}_{D,c}^{C_2} (\rho_l/\rho_g)^{(C_3+C_5)} (L_c/D_c)}, \tag{4}$$

with C_{1-5} (0.0722, −0.312, −0.644, 0.900, 0.724), D_c hydraulic diameter of channel, L_c channel length, $We_{D,c}$ Weber number $\rho_l u_l^2 D_c/\sigma$, and x_i is the pseudo-inlet quality (which represent the inlet liquid subcooling). The experimental result of [10] is presented as which is higher than predicted by Eq. (4), and is shown as $q_{CHF,FB,2}$ in Fig. 2.

The FBCW hydrodynamic limits include the perforation choking limit $q_{CHF,ch}$ (sonic flow through contraction) [16]

$$q_{CHF,ch} = c_d \frac{N_{per} \lambda_{per} W_{per}}{A_m} \left[\gamma \rho_g p_g \left(\frac{2}{\gamma + 1} \right)^{(\gamma+1)/(\gamma-1)} \right]^{1/2}, \tag{5}$$

with c_d discharge coefficient, N_{per} ratio of monolayer unit cell per perforation, λ_{per} and W_{per} perforation length and width, A_m monolayer unit cell area, γ heat capacity ratio, and p_g is vapor pressure in monolayer. This relation uses the perforation unit-cell geometry to determine the vapor speed.

The FBCW capillary-viscous limit $q_{CHF,c-v}$ is governed by capillary liquid flow through the 3-D wick (screenlayer, posts, and monolayer [17]), and in approximate closed form is

$$q_{CHF,c-v} = (p_{c,max} - \Delta p_{s,\updownarrow} - \Delta p_{s,\leftrightarrow}) \frac{\rho_l}{\mu_l} \left[\frac{H_p}{K_p A_p} + \frac{(L_p - D_p)/2}{K_m A_{m,ac}} \right]^{-1} \frac{\Delta h_{lg}}{A_e}, \tag{6}$$

with $p_{c,max}$ maximum capillary pressure in monolayer, $\Delta p_{s,\updownarrow}$ pressure drop across and $\Delta p_{s,\leftrightarrow}$ along screenlayer, μ_l liquid viscosity, H_p post height, K_p post permeability, A_p post cross-sectional area, L_p unit cell size, D_p post diameter, K_m monolayer permeability, $A_{m,ac}$ cross-sectional area of liquid flow in the monolayer in the unit cell [defined as $\pi(L_p - D_p)\langle\delta_l\rangle_m$], and A_e evaporator area. This equation is described in detail in [17].

The monolayer wick boiling limit $q_{CHF,b}$ occurring when bubbles form inside the wick due to large liquid superheat, is modeled as [19]

$$q_{CHF,sh} = \frac{\langle k \rangle_m}{\langle \delta_l \rangle_m} \Delta T_{sh,max}, \tag{7}$$

$$\Delta T_{sh,max} = \frac{T_{lg}}{\Delta h_{lg} \rho_g} \left(\frac{2\sigma}{r_{cr}} - p_{c,max} \right), \tag{8}$$

where maximum critical superheat $T_{sh,max}$ is determined by the critical nucleation site radius r_{cr} and maximum capillary pressure $p_{c,max}$ driven by meniscus curvature in the monolayer [18,19]. For conventional metallic material, r_{cr} is from 0.2 μm to 25 μm [20]. In the monolayer vapor chamber [1] where the copper particles are oxidized for improved wetting, r_{cr} is observed in order of 100 nm typical of other experiments [21]. The above wick superheat limit for the wick consider in this study is shown in Fig. 2.

Over the screenlayer saturated water flows at pressure $p_{l,o}$ (1 atm), and the vapor is injected into this stream through the screenlayer perforation undergoing pressure drop Δp_{per}. The FBCW perforation vapor pressure drop limit $q_{CHF,per}$ occurs when Δp_{per} is equal to the maximum capillary pressure $p_{c,max}$ (vapor flows through the perforations only), and the liquid–gas stability limit $q_{CHF,l-g,st}$ occurs when the liquid track becomes unstable and ruptures downstream.

The maximum conductance is when the heat transfer is limited only by the Kapitza interfacial limit [22] due to mismatch of atomic-vibrational modes of the meniscus, substrate and liquid water [23,24]. In analysis of extreme heat transfer, it is suggested that the synthetic diamond substrate is suitable and would provide the highest solid thermal conductivity and the largest structurally-stable temperature change across it and would set conductance limit [25] indicated in the Fig. 2 and is 34 MW/m^2 for conditions given in Table 1. The proposed FBCW is predicted to reach record $0.1 q_{max}$, under record conductance.

3. Pressure drops and flows in FBCW

In FBCW, the maximum capillary pressure $p_{c,max}$ in the monolayer should be large enough to overcome the pressure drops along and across the screenlayer $\Delta p_{s,\updownarrow}$ and $\Delta p_{s,\leftrightarrow}$, and along the post Δp_p and monolayer Δp_m, as well as Δp_{per}. Fig. 3 shows the liquid monolayer pressure $p_{l,m}$ at its lowest liquid thickness should give capillary pressure enabling vapor flow through the perforation at pressure

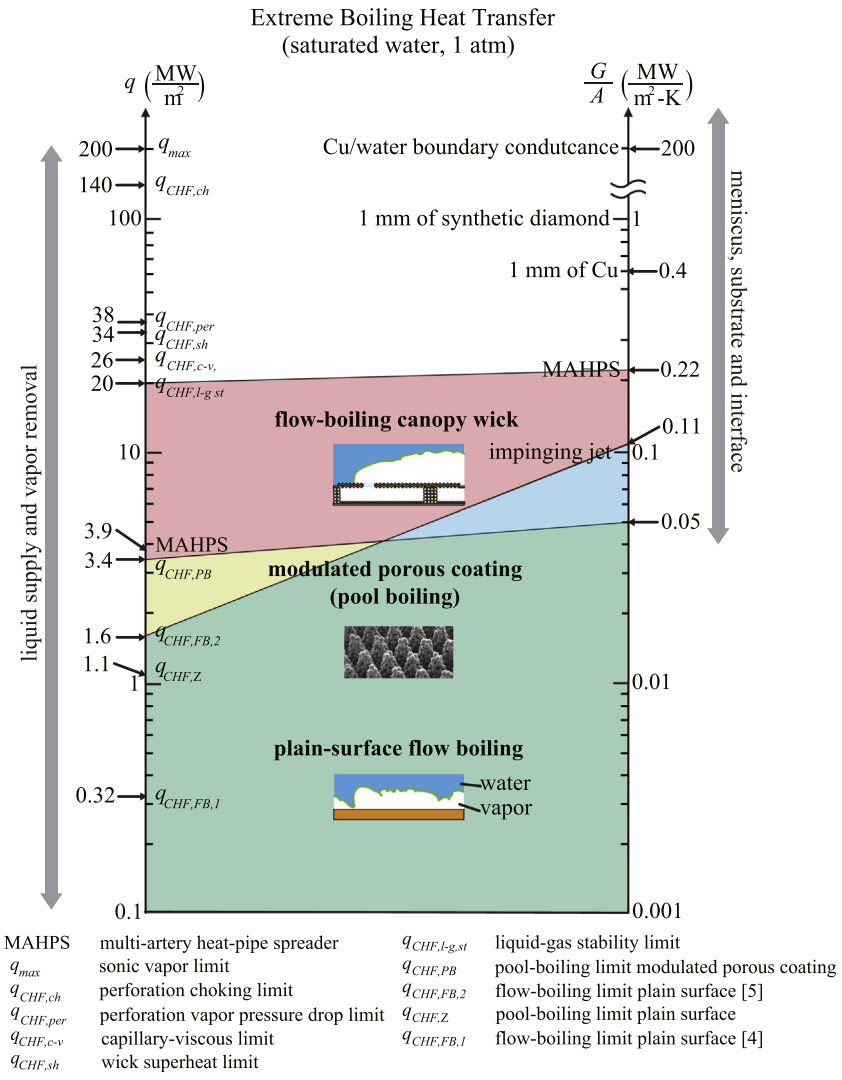

Fig. 2. Range and regimes of flow-boiling heat flux and heat transfer coefficient (G/A) for saturated water at 1 atm. The record modulated porous coated pool boiling (PB), flow boiling (FB), and multi-artery heat-pipe spreader (MAHPS) experimental results, as well as predicted performance of FBCW, are shown. The highest possible q (limited by unidirectional thermal vapor flux) and G/A (solid-liquid atomic-vibration boundary conductance) are marked. The capillary-viscous, perforation chocking and pressure drop, wick superheat, and Zuber pool boiling and plain-surface flow boiling limits are also shown.

$p_{l,o} + \Delta p_{per}$. $q_{CHF,l-g,st}$ can be reached under this condition, and details of pressure drop calculations are reported in Appendix C and [17].

The fluid dynamics of the vapor venting into the liquid stream, is governed by the inertia, viscous, buoyancy, and surface tension forces. In addition, at high heat flux the vapor flux can lead to vapor compressibility effects (not included in current analysis). Since our CFD assumes phasic incompressibility, we limit the $\mathrm{Ma}_{g,o}$ to 0.3 [26]. In FBCW, typical values of dimensionless numbers are the Reynolds (liquid l and vapor g), Weber, Froude and Mach numbers [27,28], i.e.,

$$\mathrm{Re}_l = \frac{\rho_l u_{l,o} W_l}{\mu_l}, \quad \mathrm{Re}_g = \frac{\rho_g v_{g,o} D_{per}}{\mu_g}, \quad \mathrm{We}_{D,c} = \frac{\rho_l u_{l,o}^2 D_c}{\sigma},$$
$$\mathrm{Fr}_{D,per} = \left[\frac{\rho_l u_{l,o}^2}{g(\rho_l - \rho_g) D_{per}}\right]^{1/2}, \quad \mathrm{Ma}_{g,o} = \frac{v_{g,o}}{u_a}, \tag{9}$$

which are listed in Table 1 for $q = 20\ \mathrm{MW/m^2}$, liquid inlet velocity $u_{l,o} = 2$ m/s, and geometric parameters of Fig. 1. Here D_{per} is a hydraulic diameter of perforation, and u_a is speed of sound at vapor. Characteristic lengths in the dimensionless numbers are critical length scales of liquid and vapor motions. The large $\mathrm{We}_{D,c}$ and $\mathrm{Fr}_{D,per}$ ensure dominance of liquid inertia over surface tension and buoyancy, and optimal selection of the perforation geometry ensures that vapor compressibility is not significant ($\mathrm{Ma}_{g,o} < 0.3$ [26]). In FBCW, the base channel size $[L_c(W_l + W_{per})]$ is the total monolayer area, and a perforation size ($\lambda_{per} W_{per}$) in Table 1 is determined to satisfy the pressure drop condition in Fig. 2 and to keep vapor flows incompressible. Two screen layers are used, and their specifications are introduced in detail in Table 1. Once evaporation begins, the vapor pressure exceeds the channel liquid pressure, and meniscus at the perforation is not ruptured. The volume-averaged conductance and superheat $T_s - T_{lg}$ at the monolayer ($q = 20\ \mathrm{MW/m^2}$) are calculated by [17] using $q = (G/A)(T_s - T_{lg})$ and Eq. (7), and the latter is 93 K (Table 1).

4. Results and discussion

The stable liquid track heat flux limit $q_{CHF,l-g,st}$, along with the capillary-viscous limit, determine the optimal FBCW performance (Fig. 2), and the corresponding instantaneous liquid and vapor flow fields are shown in Fig. 4 (Table 1 parameters and two axial perforations). As vapor is injected through the perforation, it spreads in x, y, and z directions and in the first few ms the vapor continues to spread in the z direction with small velocity at the exit [Fig. 4(a)].

Table 1
The $q = 20$ MW/m^2, $u_{l,o} = 2$ m/s case with geometric conditions (top row); flow dimensionless numbers (middle row); and pressure drops, thermal conductance and superheat (bottom row). Channel height H_c, perforation distance in x and y directions W_l and L_{per}, monolayer particle diameter and porosity d_m and ϵ_m, gas velocity at perforation $v_{g,o}$, and permeation liquid velocity at screenlayer $v_{l,o}$. Other wick parameters are listed in Table B1 of Appendix B. The CFD methods and verification are given in Appendix A.

q (MW/m^2)	$u_{l,o}$ (m/s)	H_c, L_c (mm)	λ_{per}, W_{per} (mm)	W_l, L_{per} (mm)	d_m/ϵ_m (mm)	$v_{g,o}/v_{l,o}$ (m/s)	$1/N_{per}$
20	2.0	15,15	5.5,1.5	5.5,1	50/0.40	96.5/0.011	8.5/2
Re_l	Re_g	$We_{D,c}$	$Fr_{D,per}$	$Ma_{g,o}$	$u_{g,o}/u_{l,o}$	ρ_l/ρ_g	μ_l/μ_g
3.8×10^4	1.1×10^4	630	13.2	0.25	48	1.6×10^3	4.6×10^{-2}
$\Delta p_{s,\updownarrow}/\Delta p_{s,\leftrightarrow}$ (kPa)	Δp_p (kPa)	Δp_m (kPa)	Δp_{per} (kPa)	$\Sigma \Delta p_i$ (kPa)	$p_{c,max}$ (kPa)	G/A (MW/m^2-K)	$T_s - T_{lg}$ (K)
0.74/0.026	1.66	13.3	5.8	21.5	21.7	0.22	93

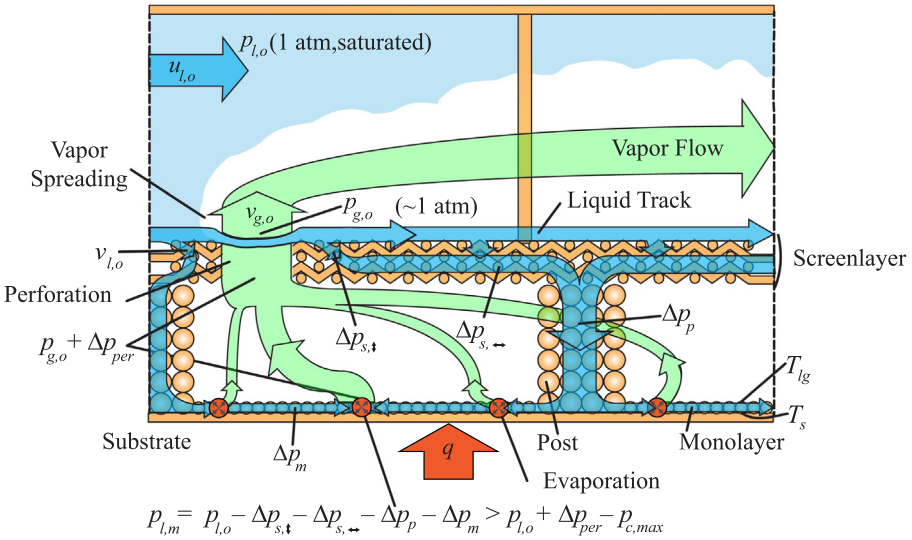

Fig. 3. Pressure distribution of the liquid and vapor phases in the wicks and in the liquid stream. q is reached to the CHF when the total pressure drop is equal to the maximum capillary pressure in the monolayer. The monolayer and perforation pressure drop dominates at high heat flux.

After this initial period, the vapor track in the z direction becomes established (with time variations), and steady exit vapor flow occurs. This wavy interface is similar to that observed in plain-surface flow boiling [8,29] and gas-sheared liquid film [30], where some vapor track breakdown happen intermittently (induced by the liquid shear) [Fig. 4(b)]. As shown in Fig. 4(c), at the exit the liquid track area A_l and width w_l in yz plane are clearly observable. The w_l and A_l are the width and cross-section area of the liquid track over the screenlayer unit cell, and w_l is along the y-direction at $z = 0$, and A_l is in the yz-plane and varies with x. For $u_{l,o} = 2$ m/s, the droplets entrained at the vapor interface can be seen [Fig. 4(c)], similar to [30]. Droplet ligaments are also formed between two neighboring fast vapor tracks similar to gas-sheared liquid film [30]. These phenomena are observed in the Video (click here, https://www.youtube.com/watch?v=xPsdDc3d-gg&feature=youtu.be). These entrained droplets join the liquid track and assist in liquid supply to the wick. In plain-surface flow-boiling, the liquid supply is obstructed by vapor blanket grown from bubbles and cause dryout [31], and FBCW defer this by marinating the narrow, periodic liquid track reaching much higher dryout limit ($q = 20$ MW/m^2). In the channel, there are two vapor track regimes; one is an isolated-vapor track, and the other is an oscillation track which has both isolated- and merged- vapor tracks. The isolated-vapor track is a state where vapor tracks have streamwise continuity while not being merged with adjacent vapor tracks. In the merged-vapor tracks, vapor tracks are combined laterally. These two types of vapor track regimes are marked in Fig. 4.

In selecting the perforation geometry, we first note that the optimal unit cell for perforation needs to match the wick unit cell formed by the posts. The periodic liquid tracks are formed along the x direction and within the perforation separation distance W_l shown in inset of Fig. 5. The variation of the time-averaged liquid track width $\overline{w_l}$ and cross-section area $\overline{A_l}$ as a function of W_l for the conditions in Table 1 are shown in this figure. For $W_l < 2.5$ mm no stable liquid track is formed, while for $W_l > 5.5$ mm the perforation flow area is reduced such that the vapor compressibility [26] and capillary viscous limits are reached. Within these limits, $\overline{w_l}$ and $\overline{A_l}$ increase with W_l. This optimal perforation geometry would result in the large liquid track width and area to ensure stable liquid supply, and this is the geometry used in the simulation.

Fig. 6(a) and (b) shows the predicted temporal variations of A_l and w_l, at three streamwise locations, for $q = 20$ MW/m^2 and $u_{l,o} = 2$ m/s with the snapshots of the liquid profile. For guiding convenience, shaded bands are marked to show the trends and continuous liquid track (along x and z directions). At the upstream of the exit, the vapor tracks emerging from the perforations remain isolated and separated by the liquid track extending to the top of the channel. With increase in x, the vapor track oscillates between the isolated and merged states, while the liquid track remains continuous liquid supply to the screenlayer. For formation of streamwise continuous liquid track between perforations, the liquid inertia should overcome the lateral vapor spreading, which in turn depends on the vapor inertia through the perforation. In addition to streamwise (x), the liquid track continuity in vertical (z) direction (larger A_l) improves the liquid supply. So, as the coverage of isolated vapor track increases, the FBCW has improved irrigation for higher heat flux of $q_{CHF,l-g,st}$ (= 20 MW/m^2). For comparison with

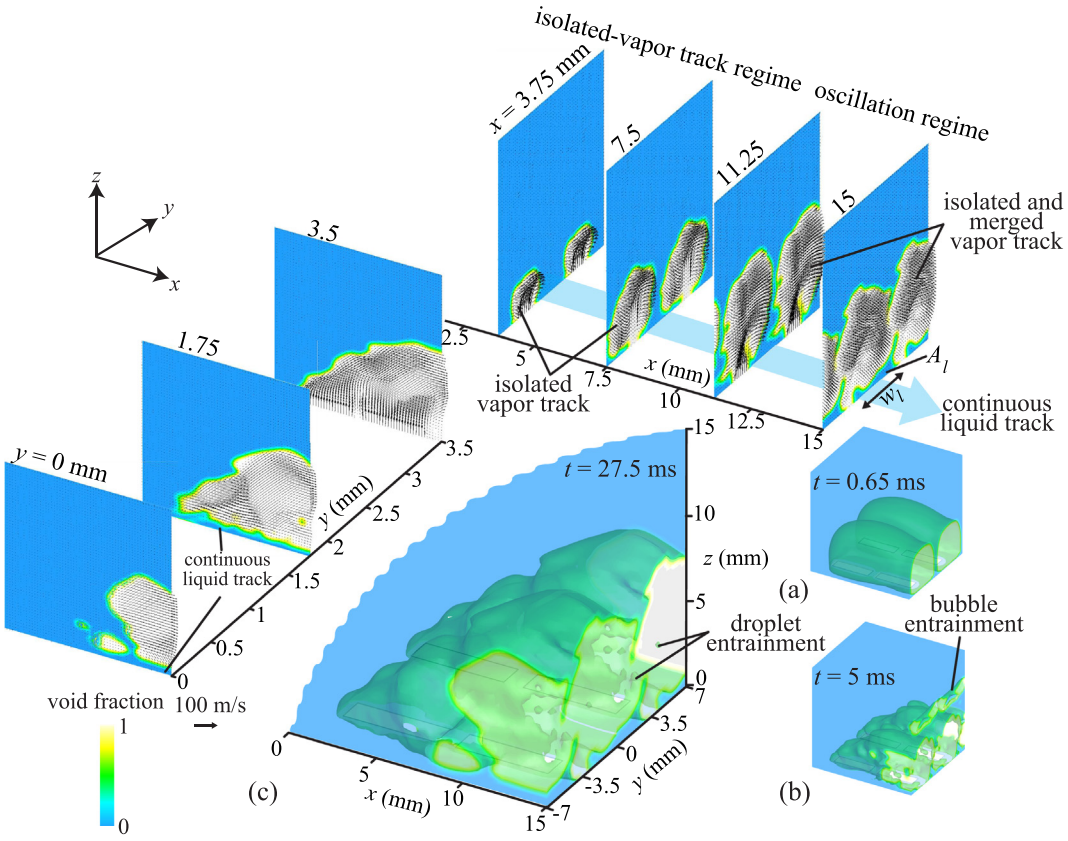

Fig. 4. Instantaneous void-fraction distribution and velocity fields at (a) t = 0.65, (b) 5, and (c) 27.5 ms, for two axial perforations, 20 MW/m^2 and 2 m/s. Cross-sectional flow fields (xz and yz planes) at different x and y positions are also shown. The video can be found here (https://www.youtube.com/watch?v=xPsdDc3d-gg&feature=youtu.be).

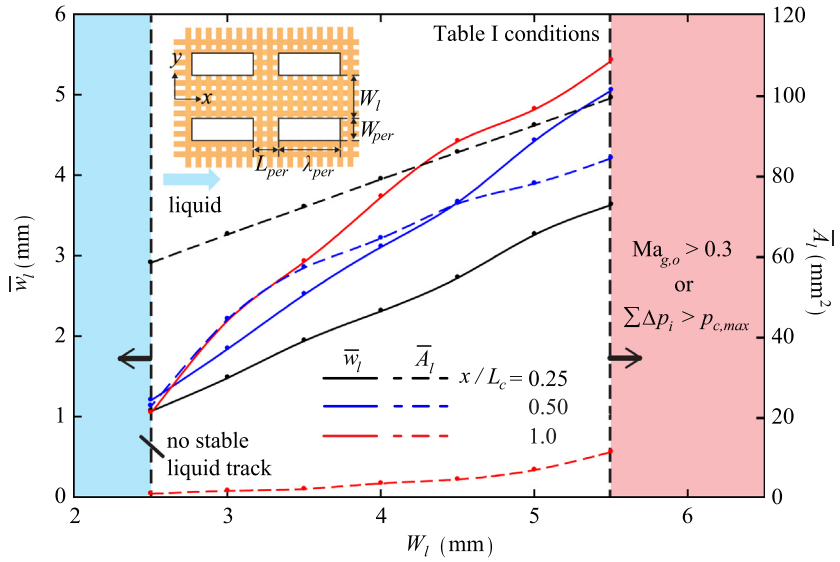

Fig. 5. Variations of the time-average liquid track width and cross-section area, at three x locations, with respect to the perforation separation distance and for conditions listed in Table 1. The other perforation parameters are also shown. To the left no stable liquid track is formed, and to the right the compressibility or the capillary-viscous limits are reached.

Fig. 6(a) and (b), the results for q = 20 MW/m^2 and $u_{l,o}$ = 1 m/s are shown in Fig. 6(c) and (d). For lower $u_{l,o}$ the isolated-vapor track regime is less sustainable, and at x = 7.5 mm, the z-direction continuity breaks down. At x = 15 mm, during the most of the time (greater than 90% of time), there is merged-vapor track state (with smaller z-direction extension), which is in the oscillation regime.

The optimal condition for continuous liquid track in x and z directions is determined from the Re_l and Re_g, giving a threshold liquid velocity $u_{l,o}$, for while satisfying the compressibility requirement. Also considering the role of viscosities, and large $\mathrm{We}_{D,c}$ and $\mathrm{Fr}_{D,per}$ (Table 1), $\mathrm{Re}_l/\mathrm{Re}_g$ controls the fate of the liquid track continuity and stability. Fig. 7 shows the extent of isolated-vapor track

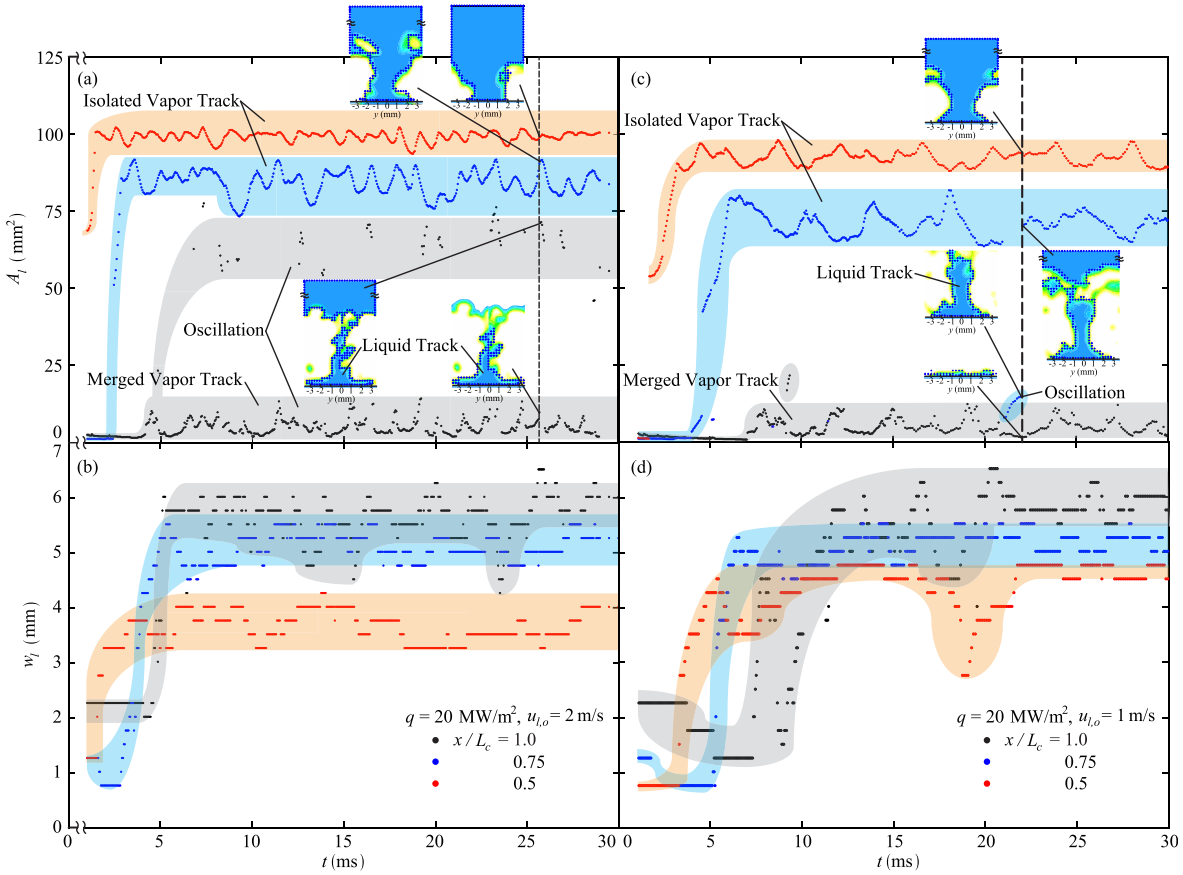

Fig. 6. For $q = 20\ \mathrm{MW/m^2}$, time variations of the predicted (a and c) A_l, and (b and d) w_l at three streamwise locations at $u_{l,o} = 2$ (a and b) and 1 (c and d) m/s. The instantaneous CFD results and shaded guiding bands are shown, as well as the snapshots of the liquid track profile. Very thin extensions are not included in w_l.

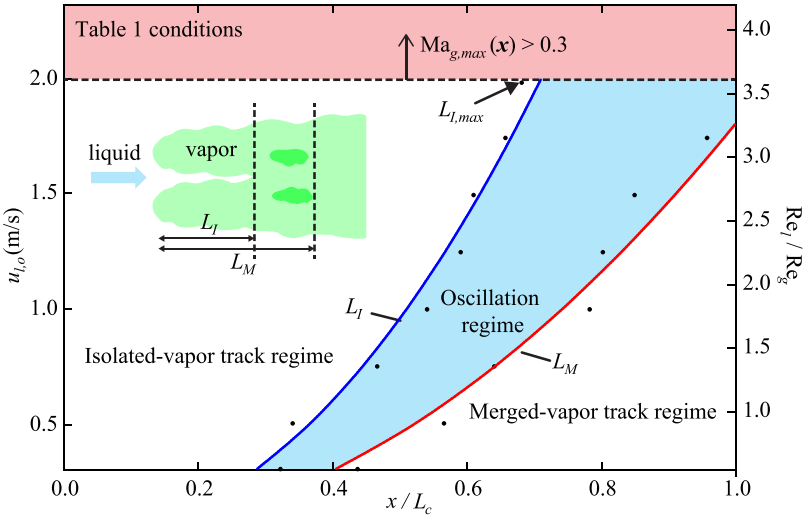

Fig. 7. Variations of the surface coverage with isolated and/or merged-vapor tracks with respect to the liquid velocity and $\mathrm{Re}_l/\mathrm{Re}_g$. The transition criterion (x-coordinate) between isolated-vapor track and oscillation regimes (L_l), and between oscillation and merged-vapor track regimes (L_M) are also marked. $\mathrm{Ma}_{g,max}(x) > 0.3$ limit is indicated, and correlated L_l/L_c and L_M/L_c are plotted.

regime L_l/L_c over the surface, as a function of liquid velocity. Larger liquid coverage occurs with larger liquid velocity, however the increase of liquid coverage diminishes as liquid velocity increases. Where the isolated-vapor track regime ends, a region where the vapor track oscillated between isolated and merged [also shown in Fig. 6(a)] begins. For lower liquid velocities, this oscillating region is followed by the merged-vapor track regime (starts at L_M/L_c), where liquid track is enclosed by the surrounding vapor flows [in Fig. 6(c)]. For liquid velocity larger than 2 m/s, the local streamwise vapor velocity become large enough so the compressibility (not included in the CFD analysis) may be significant [26], and this is also marked in Fig. 7. At $u_{l,o} = 2$ m/s, the FBCW has the

largest extent of isolated-vapor track regimes ($L_{l,max}$) under the vapor compressibility limit. From the saturated, plain-surface forced correlation [32], $q_{CHF,FB}$ is

$$\frac{q_{CHF,FB}}{\rho_l u_l \Delta h_{lg}} \sim \left(\frac{\rho_g}{\rho_l}\right)^{1/2} \mathrm{We}_{L,c}^{-1/4}, \tag{10}$$

where L_c is the characteristic length of the Weber number. Using L_i/L_c (i = I, M), we start with

$$\frac{q_{FBCW}}{\rho_l u_l \Delta h_{lg}} \sim \left(\frac{L_i}{L_c}\right)^{-a}, \tag{11}$$

and CHF occurs when bubble crowding completely covers the surface [29,31] corresponding to the merged-vapor track in FBCW. However, in FBCW, liquid track can be sustained beneath the vapor blanket by screenlayer perforation separation and capillarity, with liquid-gas stability limit of FBCW $q_{CHF,l-g,st} > q_{CHF,FB}$. In the FBCW, $q_{FBCW} = \rho_g u_g \Delta h_{lg} N_{per} \lambda_{per} W_{per}/L_c(W_{per}+W_l)$,. With $a = 1$ and using Eqs. (10) and (11), we suggest ($i = L, M$)

$$\frac{L_i}{L_c} = c_i \frac{\mathrm{Re}_l}{\mathrm{Re}_g}\left(\frac{\rho_g}{\rho_l}\right)^{1/2} \mathrm{We}_{L,c}^{-1/4} \times \frac{A_m}{N_{per}\lambda_{per}W_{per}} \frac{\mu_l}{\mu_g}\frac{D_{per}}{W_l}, \tag{12}$$

with coefficient c_i fitted with the least squares method to the numerical results in Fig. 7, which are 0.37(c_l) and 0.54 (c_M). The CFD methods and verification are described in Appendix A.

5. Conclusions

We have shown that FBCW, a boiling metamedium, enables extreme heat transfer by controlling heat transfer/vapor generation and hydrodynamics of the vapor and liquid tracks. FBCW separates and directs these tracks to ensure the highest liquid supply rate and smallest thermal resistance. Heat flux up to $0.1q_{max}$ is predicted, and the increase of the liquid velocity extends the isolated-vapor track coverage, and gradually leads to the streamwise local vapor compressibility limit. The FBCW transforms boiling heat transfer using unit-cell, 3-D capillary structure under saturated liquid flow and is capable of achieving record fraction of the theoretical maximum heat flux limit.

Conflict of interest

None declared.

Acknowledgment

This work is supported by NSF – USA (Thermal Transport and Processes, CBET16235720).

Appendix A. CFD Methods

The liquid supply and monolayer evaporation are modeled as described in [17], using numerical solutions to (i) the point-wise Navier–Stokes and energy equations and the principles of meniscus minimum-surface energy, and (ii) local volume-average momentum and energy equations in the porous media. Here the two-phase channel flow is solved using ANSYS FLUENT with the volume of fluid (VOF) method [33] under incompressibility, i.e., solving [34,35]

$$\frac{\partial \rho}{\partial t} + \nabla \cdot \mathbf{u} = 0 \tag{A1}$$

$$\frac{\partial}{\partial t}(\rho \mathbf{u}) + \nabla \cdot (\rho \mathbf{u}\mathbf{u}) = -\nabla p + \nabla \cdot [\mu(\nabla \mathbf{u} + \nabla \mathbf{u}^T)] + \rho \mathbf{g} + \mathbf{f}_s, \tag{A2}$$

with velocity $\mathbf{u}$, pressure p, surface tension force $\mathbf{f}_s$, and mixture density ρ and dynamic viscosity μ. The liquid-gas mixture is treated as compressible while each phase is assumed as incompressible. The vapor volume fraction α equation and mixture properties are

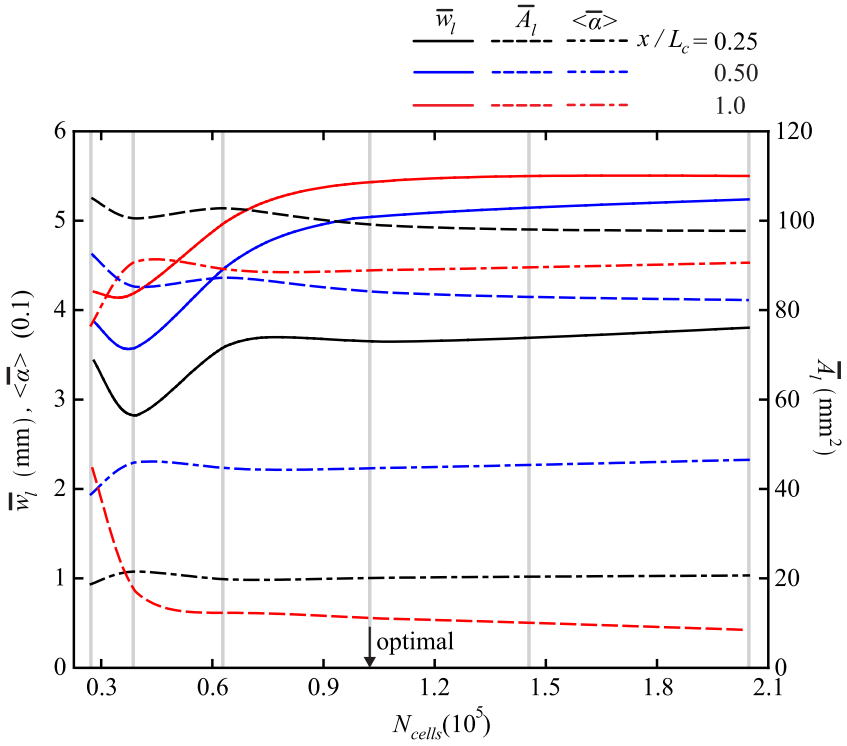

Fig. A1. Variations of key quantities, namely the time-averaged liquid track width and area, and cross-section and time-averaged void fraction, as a function of number of computational cells, for q = 20 MW/m^2 and $u_{l,o}$ = 2 m/s. The results show using 10^5 cells would lead to no mesh-size dependence.

Table B1
The wick geometric parameters [17]: monolayer d_m, ϵ_m, L_p and θ_c (particle diameter, porosity, post pitch and contact angle); post d_p, ϵ_p, D_p, H_p, and K_p (particle diameter, porosity, height, and permeability); screenlayer $d_{s,sh}$, $d_{s,wa}$, $D_{s,po}$ and $n_{sh} \times n_{wa}$ (diameters, pore size, and number density of shute and warp wires).

Monolayer		Post		Screenlayer	
d_m	50 μm	d_p/ϵ_p	150 μm/0.35	$d_{s,sh}$	66 μm
ϵ_m	0.40	D_p	2.2 mm	$d_{s,wa}$	66 μm
L_p	3.5 mm	H_p	2.6 mm	$D_{s,po}$	0.10 mm
θ_c	45°	K_p	12.7 μm^2	$n_{sh} \times n_{wa}$	145 × 145/in^2

$$\frac{\partial}{\partial t}(\alpha\rho_g) + \nabla\cdot(\alpha\rho_g\mathbf{u}_g) = 0 \tag{A3}$$

$$\rho = \alpha\rho_g + (1-\alpha)\rho_l, \qquad \mu = \alpha\mu_g + (1-\alpha)\mu_l. \tag{A4}$$

The continuum surface force $\mathbf{f}_s$ model [36] is

$$\mathbf{f}_s = \sigma\frac{\rho\kappa_g\nabla\alpha}{\frac{1}{2}(\rho_g+\rho_l)}, \tag{A5}$$

where $\kappa_g = \nabla\cdot(\nabla\alpha/\alpha)$, which is the interface curvature (interface normal defined as gradient of vapor volume fraction).

The vapor interface reconstruction used the geometric reconstruction scheme [37], and the SIMPLE scheme is applied for the pressure-velocity coupling. The quadrilateral mesh is used with uniform grid size of 0.25 mm, and the mesh-size independence is tested using progressively smaller mesh size (Fig. A1). A typical perforation size (two perforations, 5.5 × 1.5 mm^2) in a computational domain (15 × 15 × 7 mm^3)] with two prism layers (growth ratio of 1.2) is applied to the top and bottom boundaries. The channel height H_c is selected for a boundary-layer liquid flow behavior (i.e., independent of channel height, while avoiding very long computing time). When H_c is extended by 40%, A_l in oscillating regime changes by 3.6% (merged-vapor track) and 5.6% (isolated-vapor track with consideration of cross-section area extension). w_l also changes within 2%. Liquid velocity $u_{l,o}$ toward inside the domain (x direction) is given to liquid inlet. Liquid velocity $v_{l,o}$ flowing into screenlayer (negative z direction) is

$$v_{l,o} = \frac{\dot{m}_e}{\rho_l A_m(1-1/N_{per})}, \tag{A6}$$

where $\dot{m}_e = qA_m/\Delta h_{lg}$, Δh_{lg} is heat of evaporation, A_m is monolayer unit cell area, and $\dot{m}_e$ is mass flow rate of evaporation. Perforation vapor velocity $v_{g,o}$ is

$$v_{g,o} = \frac{\dot{m}_e}{\rho_g(2\lambda_{per}W_{per})}. \tag{A7}$$

As shown in Table 1, there is vapor pressure drop across the perforation and the vapor density change accordingly, but this is neglected in the current calculations. Periodic boundary conditions are imposed to the side surfaces, top wall has no-slip condition, and outflow condition is defined at the outlet.

To ensure the numerical results are independent of grid size, progressively larger number of computational cells were used, and Fig. A1 shows that with 10^5 cells the results will become independent of the mesh size. The results are for q = 20 MW/m^2 and $u_{l,o}$ = 2 m/s, and show the variations in the time-averaged liquid track width and area, and cross-section and time-averaged void fraction, at three different streamwise locations.

Appendix B. Wick geometric parameters

The optimized geometric parameters (marked in Fig. 1) of the FBCW are listed in Table B1 and are based on the MAHPS design reported in [17]. The detail of the porous-media flow and heat transport analyses and validations are given in [17].

Appendix C. Pressure drop relations

Since the vapor passes only through the perforations, the screenlayer is a perforated finite thickness plate. For $0.006 < \beta < 0.75$ and $H_s/D_{per} < 0.8$, the pressure drop through the perforated plate [38] is

$$\Delta p_{per} = \frac{1}{2}\rho_g u_{g,m}^2 \times \left[\frac{1.642}{\beta(1-\beta^{2.6})\left(1+\overline{l_1}^{3.5}+\beta^{3.6}\right)} - 1\right]^2 - \rho_g g H_s, \tag{C1}$$

with $\overline{l_1} = H_s/D_{per}$, H_s screenlayer thickness, D_{per} hydraulic diameter of perforation, $u_{g,m}$ vapor velocity before perforation, and β ratio

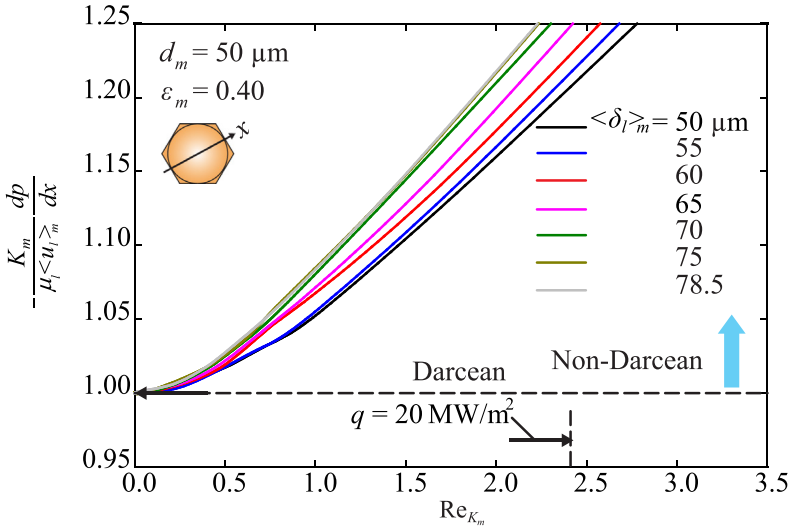

Fig. C1. Variations of dimensionless monolayer unit-cell pressure drop with respect to Re_{K_m}, for different liquid thickness $\langle\delta_l\rangle_m$. Re_{K_m} range of q = 20 MW/m^2 is also marked.

of perforation area to area before it. Idelchik [39] suggested another empirical correlation

$$\Delta p_{per} = \frac{\rho_g u_{g,m}^2}{2\beta^2}\left[\frac{(1-\beta)^{0.75}}{2} + (2.4-\overline{l_1})^{\overline{l_2}}(1-\beta)^{1.375} + (1-\beta)^2 + f\overline{l_1}\right] - \rho_g g H_s, \tag{C2}$$

with $\overline{l_2}$ and friction coefficient f as

$$\overline{l_2} = 0.25 + \left(\frac{0.535\overline{l_1}^8}{0.05+\overline{l_1}^7}\right), \qquad f = \frac{0.316}{\mathrm{Re}_g^{0.25}}. \tag{C3}$$

In Eqs. (C1)–(C3), the hydrostatic pressure drop by gravitational force is also included, and both correlations give very close results.

In [17], the monolayer with closely hexagonal-packed particles d_m = 50 μm and ϵ_m = 0.40 gives optimal performance over a range of heat flux, and this geometry is also adopted in this study. Using the minimum-surface energy principle, the meniscus topology is obtained using the Surface Evolver. Since the monolayer Weber number $\mathrm{We}_m = \rho_l \langle u_l\rangle_m^2 \langle \delta_l\rangle_m/\sigma$ and capillary number $\mathrm{Ca}_m = \mu_l\langle u_l\rangle_m/\sigma$ are small, so the static meniscus is used. Detailed processes and results are explained in [17]. In the monolayer, for low heat flux, the liquid Reynolds number $\mathrm{Re}_{l,m} \ll 1$, and pressure drop $\Delta p_{l,m}$ varies linearly with velocity $\langle u_l\rangle_m$ (Darcean flow). For $\mathrm{Re}_{l,m}$ of $O(1)$ at high heat flux used here, the so-called Forchheimer (non-Darcean) range, the quadratic $\langle u_l\rangle_m$ term [40–43] for $\Delta p_{l,m}$ is presented with the permeability-based Reynolds number $\mathrm{Re}_{K_m} = \rho_l\langle u_l\rangle_m K_m^{1/2}/\mu_l$

$$-\frac{K_m}{\mu_l\langle u_l\rangle_m}\frac{dp_{l,m}}{dx} = c_{F,1} + c_{F,2}\mathrm{Re}_{K_m}, \tag{C4}$$

with $dp_{l,m}/dx$ liquid pressure gradient, and K_m permeability. The dimensionless pressure gradient across the unit cell shown in Fig. C1 is calculated by ANSYS FLUENT, and covers the Darcy and Forchheimer regimes. Here $C_{F,1}$ = 1 as used in [44,41,43], and for given range of $\mathrm{Re}_{l,m}$, $C_{F,2}$ is comparable to empirical results from experiments [45,44,40]. The results show that the meniscus liquid film thickness $\langle\delta_l\rangle_m$ influences $C_{F,2}$ under laminar flow condition (monolayer Reynolds number $\mathrm{Re}_{l,m} < 200$) [40].

Appendix D. Supplementary material

Supplementary data associated with this article can be found, in the online version, at https://doi.org/10.1016/j.ijheatmasstransfer.2017.10.079. The video can be found here (https://www.youtube.com/watch?v=xPsdDc3d-gg&feature=youtu.be).

References

[1] G.S. Hwang, Y. Nam, E. Fleming, P. Dussinger, Y.S. Ju, M. Kaviany, Multi-artery heat pipe spreader: experiment, Int. J. Heat Mass Transfer 53 (13-14) (2010) 2662–2669, https://doi.org/10.1016/j.ijheatmasstransfer.2010.02.046.

[2] S.G. Liter, M. Kaviany, Pool-boiling CHF enhancement by modulated porous-layer coating: theory and experiment, Int. J. Heat Mass Transfer 44 (22) (2001) 4287–4311, https://doi.org/10.1016/S0017-9310(01)00084-9.

[3] D. Cooke, S.G. Kandlikar, Effect of open microchannel geometry on pool boiling enhancement, Int. J. Heat Mass Transfer 55 (4) (2012) 1004–1013, https://doi.org/10.1016/j.ijheatmasstransfer.2011.10.010.

[4] Z.G. Qu, Z.G. Xu, C.Y. Zhao, W.Q. Tao, Experimental study of pool boiling heat transfer on horizontal metallic foam surface with crossing and single-directional V-shaped groove in saturated water, Int. J. Multiph. Flow 41 (2012) 44–55, https://doi.org/10.1016/j.ijmultiphaseflow.2011.12.007.

[5] C.M. Patil, S.G. Kandlikar, Pool boiling enhancement through microporous coatings selectively electrodeposited on fin tops of open microchannels, Int. J. Heat Mass Transfer 79 (2014) 816–828, https://doi.org/10.1016/j.ijheatmasstransfer.2014.08.063.

[6] A. Jaikumar, S.G. Kandlikar, Ultra-high pool boiling performance and effect of channel width with selectively coated open microchannels, Int. J. Heat Mass Transfer 95 (2016) 795–805, https://doi.org/10.1016/j.ijheatmasstransfer.2015.12.061.

[7] S. Mori, Y. Utaka, Critical heat flux enhancement by surface modification in a saturated pool boiling: a review, Int. J. Heat Mass Transfer 108 (2017) 2534–2557, https://doi.org/10.1016/j.ijheatmasstransfer.2017.01.090.

[8] J.C. Sturgis, I. Mudawar, Critical heat flux in a long, rectangular channel subjected to one-sided heating-I. Flow visualization, Int. J. Heat Mass Transfer 42 (10) (1999) 1835–1847, https://doi.org/10.1016/S0017-9310(98)00274-9.

[9] D.D. Hall, I. Mudawar, Critical heat flux (CHF) for water flow in tubes-I. Subcooled CHF correlations, Int. J. Heat Mass Transfer 43 (14) (2000) 2605–2640, https://doi.org/10.1016/S0017-9310(99)00192-1. <http://www.sciencedirect.com/science/article/pii/S0017931099001921>.

[10] L. Wang, A.R. Khan, N. Erkan, H. Gong, K. Okamoto, Critical heat flux enhancement on a downward face using porous honeycomb plate in saturated flow boiling, Int. J. Heat Mass Transfer 109 (2017) 454–461, https://doi.org/10.1016/j.ijheatmasstransfer.2017.01.113.

[11] S.G. Lee, M. Kaviany, C.-J. Kim, J. Lee, Quasi-steady front in quench subcooled-jet impingement boiling: experiment and analysis, Int. J. Heat Mass Transfer 113 (2017) 622–634.

[12] M. Kaviany, Principles of Convective Heat Transfer, second ed., Springer, New York, 2001.

[13] R.W. Schrage, A Theoretical Study of Interface Mass Transfer, Columbia University Press, New York, 1953.

[14] G. Standart, Z. Cihla, Interphase transport processes. I. Schrage's theories, Collect. Czechosl. Chem. Commun. 23 (1958) 1608–1618.

[15] W.R. Gambill, J.H. Lienhard, An upper bound for the critical boiling heat flux, ASME J. Heat Transfer 111 (August) (1989) 815–818.

[16] D.W. Green, R.H. Perry, Perry's Chemical Engineers' Handbook, eighth ed., McGraw-Hill, New York, 2007.

[17] M. Kim, M. Kaviany, Multi-artery heat-pipe spreader: monolayer-wick receding meniscus transitions and optimal performance, Int. J. Heat Mass Transfer 112 (2017) 343–353.

[18] S. Chi, Heat Pipe Theory and Practice: A Sourcebook, Hemisphere Publishing Coporation, Washington, 1976.

[19] G.P. Peterson, An Introduction to Heat Pipes: Modeling, Testing, and Applications, John Wiley, Inc., New York, 1994.

[20] P.D. Dunn, D.A. Reay, Heat Pipes, Pergamon, New York, 1982.

[21] G.S. Hwang, E. Fleming, B. Carne, S. Sharratt, Y. Nam, P. Dussinger, Y.S. Ju, M. Kaviany, Multi-artery heat-pipe spreader: lateral liquid supply, Int. J. Heat Mass Transfer 54 (11–12) (2011) 2334–2340, https://doi.org/10.1016/j.ijheatmasstransfer.2011.02.029.

[22] M. Kaviany, Heat Transfer Physics, second ed., Cambridge University Press, New York, 2014.

[23] M.E. Caplan, A. Giri, P.E. Hopkins, Analytical model for the effects of wetting on thermal boundary conductance across solid/classical liquid interfaces, J. Chem. Phys. 140 (15) (2014) 154701.

[24] T. Vo, B. Kim, Interface thermal resistance between liquid water and various metallic surfaces, Int. J. Precis. Eng. Manuf. 16 (7) (2015) 1341–1346, https://doi.org/10.1007/s12541-015-0176-0.

[25] J.H. Lienhard, A. Khounary, Liquid jet impingement cooling with diamond substrates for extremely high heat flux applications, in: Proceedings of SPIE's International Symposium on Optics, Imaging, and Instrumentation, vol. 1997, San Diego, 1993.

[26] F. White, Fluid Mechanics, seventh ed., McGraw-Hill, New York, 2011.

[27] Y. Murai, Frictional drag reduction by bubble injection, Exp. in Fluids 55 (7) (2014) 1773.

[28] D. Kim, P. Moin, Direct Numerical Study of Air Layer Drag Reduction Phenomenon Over a Backward-Facing Step, Tech. rep., Center for Turbulence Reserach, Stanford University, 2010.

[29] C. Konishi, I. Mudawar, M.M. Hasan, Investigation of localized dryout versus CHF in saturated flow boiling, Int. J. Heat Mass Transfer 67 (2013) 131–146, https://doi.org/10.1016/j.ijheatmasstransfer.2013.07.082.

[30] A.V. Cherdantsev, D.B. Hann, B.J. Azzopardi, Study of gas-sheared liquid film in horizontal rectangular duct using high-speed LIF technique: three-dimensional wavy structure and its relation to liquid entrainment, Int. J. Multiph. Flow 67 (2014) 52–64, https://doi.org/10.1016/j.ijmultiphaseflow.2014.08.003.

[31] M. Bruder, G. Bloch, T. Sattelmayer, Critical heat flux in flow boiling-review of the current understanding and experimental approaches, Heat Transfer Eng. 38 (3) (2017) 347–360, https://doi.org/10.1080/01457632.2016.1189274.

[32] Y. Katto, C. Kurata, Critical heat flux of saturated convective boiling on uniformly heated plates in a parallel flow, Int. J. Multiph. Flow 6 (6) (1980) 575–582, https://doi.org/10.1016/0301-9322(80)90052-X.

[33] C.W. Hirt, B.D. Nichols, Volume of fluid (VOF) method for the dynamics of free boundaries, J. Comput. Phys. 39 (1) (1981) 201–225.

[34] E. Delnoij, J.A.M. Kuipers, W.P.M. van Swaaij, Computational fluid dynamics applied to chemical reaction engineering, Adv. Chem. Eng. 24 (97) (1998) 227–328.

[35] D. Ma, M. Liu, Y. Zu, C. Tang, Two-dimensional volume of fluid simulation studies on single bubble formation and dynamics in bubble columns, Chem. Eng. Sci. 72 (2012) 61–77, https://doi.org/10.1016/j.ces.2012.01.013.

[36] J.U. Brackbill, D.B. Kothe, C. Zemach, A continuum method for modeling surface tension, J. Comput. Phys. 100 (2) (1992) 335–354, https://doi.org/10.1016/0021-9991(92)90240-Y.

[37] D.L. Youngs, Numerical Methods for Fluid Dynamics, Academic Press, New York, 1982.

[38] A.J. Ward-Smith, Internal Fluid Flow, Clarendon Press, Oxfod, 1980.
[39] I.E. Idelchik, Handbook of Hydraulic Resistance, third ed., CRC Press, Florida, 1994.
[40] R.M. Fand, B.Y.K. Kim, A.C.C. Lam, R.T. Phan, Resistance to the flow of fluids through simple and complex porous media whose matrices are composed of randomly packed spheres, J. Fluids Eng. 109 (3) (1987) 274, https://doi.org/10.1115/1.3242660.
[41] I. Kececioglu, Y. Jiang, Flow through porous media of packed spheres saturated with water, J. Fluids Eng. 116 (1) (1994) 164–176, https://doi.org/10.1115/1.2910229. <http://www.osti.gov/energycitations/product.biblio.jsp?osti_id=7113838%5Cnhttp://apps.isiknowledge.com/InboundService.do?product=WOS&action=retrieve&SrcApp=AIP&UT=A1994NE37400026&SID=W2O1hGleDhnFM@O3jhf&mode=FullRecord&DestFail=http://www.isiknowledge.com>.
[42] M. Kaviany, Principles of Heat Transfer in Porous Media, second ed., Springer New York, New York, 1995, https://doi.org/10.1007/978-1-4612-4254-3. <http://link.springer.com/book/10.1007%2F978-1-4612-4254-3>.
[43] J.L. Lage, B.V. Antohe, D.A. Nield, Two types of nonlinear pressure-drop versus flow-rate relation observed for saturated porous media, J. Fluids Eng. 119 (3) (1997) 700–706, https://doi.org/10.1115/1.2819301. <http://link.aip.org/link/?JFG/119/700/1>.
[44] I.F. Macdonald, M.S. El-Sayed, K. Mow, F.A.L. Dullien, Flow through porous media-the Ergun equation revisited, Ind. Eng. Chem. Fund. 18 (3) (1979) 199–208, https://doi.org/10.1021/i160071a001. <http://pubs.acs.org/doi/abs/10.1021/i160071a001>.
[45] S. Ergun, Fluid flow through packed columns, Chem. Eng. Prog. 48 (1952) 89–94.